

Scaling Up Microfluidic Aluminum-Air Cell with Electrochemical Impedance Spectroscopy (EIS) Assisted Performance Analysis

Citation for published version:

Chen, B, Leung, DYC, Wang, H & Xuan, J 2016, 'Scaling Up Microfluidic Aluminum-Air Cell with Electrochemical Impedance Spectroscopy (EIS) Assisted Performance Analysis', *Journal of The Electrochemical Society*, vol. 163, no. 9, pp. F1032-F1037. <https://doi.org/10.1149/2.0501609jes>

Digital Object Identifier (DOI):

[10.1149/2.0501609jes](https://doi.org/10.1149/2.0501609jes)

Link:

[Link to publication record in Heriot-Watt Research Portal](#)

Document Version:

Peer reviewed version

Published In:

Journal of The Electrochemical Society

General rights

Copyright for the publications made accessible via Heriot-Watt Research Portal is retained by the author(s) and / or other copyright owners and it is a condition of accessing these publications that users recognise and abide by the legal requirements associated with these rights.

Take down policy

Heriot-Watt University has made every reasonable effort to ensure that the content in Heriot-Watt Research Portal complies with UK legislation. If you believe that the public display of this file breaches copyright please contact open.access@hw.ac.uk providing details, and we will remove access to the work immediately and investigate your claim.

**Scaling up microfluidic aluminum-air cell with electrochemical impedance spectroscopy
(EIS) assisted performance analysis**

Binbin Chen^a, Dennis Y.C. Leung^{a,*}, Huizhi Wang^b, Jin Xuan^{b,**}

^aDepartment of Mechanical Engineering, The University of Hong Kong, Pokfulam Road, Hong Kong

^bSchool of Engineering & Physical Sciences, Heriot-Watt University, Edinburgh EH14 4AS, United Kingdom

*Corresponding authors, ycleung@hku.hk (D.Y.C. Leung); j.xuan@hw.ac.uk (J. Xuan)

Abstract

Microfluidic fuel cell is a promising power source in many applications, such as portable electronic devices. In this work, a novel and unique scale-up approach is developed to increase the capability of the microfluidic aluminum-air fuel cell, while maintaining the co-laminar flow characteristic at the same time. In the scaled-up cell, the crossover of different electrolyte streams was well controlled and a higher cell output was achieved. With a four-fold increase in the electrode area, the maximum current density could be maintained over 75%. Impedance spectroscopy study on full aluminum-air cells was conducted for the first time, and employed to analyze the cell properties during their scaling up process.

1. Introduction

Among all kinds of electrochemical energy converting devices, fuel cells feature high energy densities and conversion efficiencies.¹ Most fuel cells developed to date require physical barriers, such as proton exchange membranes (PEM) or anion exchange membrane (AEM), to prevent the crossover of reactants.² Microfluidic fuel cells (MFC), in contrast, utilize the hydrodynamics of co-laminar flow, providing a possibility to overcome this issue.³ In a low Reynolds number regime with a small ratio of inertial to viscous force, MFC are able to maintain an interface to separate different streams flowing side-by-side, acting as a virtual membrane in MFC.⁴ The mixing exists only due to the relatively low diffusion rates, eliminating the use of a conductive membrane. This fluidic dynamics has also been proposed for applications in patterning,⁵ T-sensors,⁶ and lab-on-chip,⁷ etc.

The cells with membraneless design avoid many membrane-related issues, including membrane humidification, degradation and liquid water management.⁸ Furthermore, the virtual-membrane configuration allows the reactants on anodic and cathodic side to be chosen independently, offering greater flexibility with fuel and oxidant selection, thus, providing the chance to further improve reaction rates and cell voltages.⁹ With the respect of fuel and oxidant selections, different types of MFC including hydrogen-oxygen,¹⁰ formic acid-hydrogen peroxide,¹¹ methanol-oxygen,¹² vanadium species¹³ and metal-air¹⁴ fuel cells have been developed. Another significant advantage associated with MFC is their low cost. MFC can be manufactured by inexpensive methods and materials without the need of the expensive membrane.¹⁵

Scaling up of MFC is important in providing a sizeable power output for practical applications. However, it remains a challenge because in order to maintain the co-laminar flow

function, the size of the device is limited, which directly impacts the cell output. Scale-up of MFC was firstly investigated by Kjeang et al. in 2007.¹⁶ Since then, different approaches to improve the power output of MFC have been demonstrated. The most commonly used one was employing porous electrodes.¹⁶⁻²⁰ The use of three-dimensional porous electrodes considerably increases the area of reaction sites on the electrode-electrolyte contacting surface. Another flow through scaling up solution was investigated by Moore et al.²¹ The design showed a good capability of scaling up. However, the performance was found to be predominantly limited by high ohmic resistance. Cell stack has also been proposed as a way to increase power output, in which cell arrays were connected in series with fluidic electrolytes.²²⁻²⁶ However, it required a more complicated system design for liquid flow and distribution control. The scale-up of MFC in a volumetrically efficient manner remains a challenge.

In this study, a direct dimensional scaling up method of dislocated double-layer structure was proposed, based on a dual-electrolyte microfluidic aluminum (Al) -air fuel cell. The feasibility of this scaling up method was first proven. Then, the performances of cells scaled-up at different levels were investigated. In order to characterize electrical loss during scaling up of cells, EIS analysis, a powerful diagnostic tool to identify fundamental physiochemical processes in fuel cells,²⁷ was used to reveal more detailed cell properties evolution information. By employing equivalent circuit models, the underlying process and performance loss pathways were identified and quantified.²⁸ For Al-air cell, EIS has only been applied to study electrochemical processes of either Al oxidation or oxygen reduction in three-electrode systems.²⁹⁻³² Few studies have incorporated the EIS technique to investigate the full fuel cell performance. The EIS section aims at providing a premier EIS analysis on full Al-air cell. The accuracy of the analysis was verified by fitting EIS curves of cells under different conditions with the proposed equivalent circuit. The

loss during scaling up was then characterized by quantifying the parameters of elements in the equivalent circuit.

2. Experiment

2.1 Cell Design and Fabrication

Figure 1 shows the schematic of the dislocated double-layer scaling up MFC structure adopted in this work. This new design evolved from the conventional face-to-face microfluidic platform. It consists of two polymethylmethacrylate (PMMA) channel layers, sandwiched by two polyvinyl chloride (PVC) electrode layers on the top and bottom. PVC plates are employed for the electrode layers since their thickness could be as thin as 0.1 mm, ensuring a good contact between electrode and electrolyte. Each channel layer has a thickness of 0.5 mm.

A streamlined channel configuration is designed to aid the establishment of co-laminar flow in the channel. Two channel layers constitute a double-layer structure (shown in the inset in Figure 1), with a 2 mm wide interface at the converged segment. For scaling up, each channel is able to be widened (to 4 ~ 10 mm in this study) in one direction. Compared with conventional face-to-face MFC, cells with the 2 mm wide converged segment are able to maintain the interface of different streams in a larger channel. At each top and bottom layer, a rectangular window, with an area of channel width with a multiplication of 5 mm, is cut out to allow the electrodes to contact with electrolyte. Thus, the electrode area would increase at the same time during scaling up. The top layer also seals the assembly with two inlets and an outlet for fluidic electrolyte access. The structures on PMMA and PCV plates are cut by carbon dioxide laser ablation system (VLS 2.30, Universal Laser System, USA). Different layers are adhered with each other by double-side adhesive tape. The electrolyte is pumped into the cell by a syringe

pump (LSP02-1B, LongerPump, China), via 1.5 mm tubing bonded to the ports with quick dry epoxy. The flow rates of electrolyte increase linearly with the scaling of the cells, from 600 $\mu\text{l}/\text{min}$ for 2 mm, to 3000 $\mu\text{l}/\text{min}$ for 10 mm, to make sure that electrolyte flow condition is similar in cells with different channel width.

2.2 Chemicals

Electrolytes of aqueous KOH and H_2SO_4 solutions with different concentrations were prepared by dissolving KOH pillars ($\geq 85\%$, Sigma Aldrich, Hong Kong) and H_2SO_4 (95-97%, Sigma Aldrich, Hong Kong) in 18.2 M Ω deionized water (Barnstead, NANOpure DiamondTM, USA). Commercial electrodes were used in all the experiments with 99.9% Al (Guantai Metal Company, China), as anode and a gas diffusion electrode (GDE) with catalyst loading of 2 mg/cm^2 Pt/C (Hesen, China) as cathode. The properties of the GDE have been described elsewhere.³³

2.3 Electrochemical testing

Electrochemical measurements were carried out under room temperature and ambient atmospheric pressure. Each test was conducted on a new cell to make sure same conditions were applied, avoiding the influence of Al consumption. The polarization curves were obtained by potentiostatic current measurement, at every 0.2 V for 1 min from 0 V to open-circuit voltage (OCV) by a CHI 660E electrochemical workstation (Shanghai Chenhua Instruments Co., Ltd., China). The average value of the current data in the last 30 seconds of the sampling was used to represent the cell current at a certain voltage. The electrolytes used here were 1 M KOH solution (anolyte) and 1 M H_2SO_4 (catholyte). An external Ag/AgCl(in saturated KCl) electrode (Shanghai Leici Co., Ltd., China) was used as a reference electrode to acquire the single-

electrode potentials of the cells. The data of potential was recorded *in situ* by a digital multi-meter (15B, Fluke Corporation, USA).

In order to verify the accuracy of the EIS analysis on the full Al-air cell, two groups of EIS experiments were performed by changing the anolyte and catholyte individually in cells with 6 mm wide channel as listed in Table 1. The co-laminar flow configuration allows easy change of the electrolyte for each electrode. All EIS testing were recorded in a frequency range of 100 kHz to 1 Hz, with A.C. signal amplitude of 5 mV, at the voltage of peak-power density (i.e. 1.4 V for dual-electrolyte cell and 0.8 V for single-electrolyte cell). A fitting program of ZView was employed for fitting experimental EIS curves with equivalent circuit to obtain the associated parameters for each element.

3. Result and discussion

3.1 Scaling up performance characterization

Figure 2 compares the polarization curves between the conventional face-to-face and our newly designed dislocated double-layer microfluidic Al-air fuel cells with 6 mm wide channel (electrode area: 6 mm × 5 mm). The performance of the cell with 2 mm wide channel (electrode area: 2 mm × 5 mm) was tested as a benchmark. The OCV of the cell achieves 2.29 V, with a cathodic potential of 0.72 V and an anodic potential of -1.57 V vs the Ag/AgCl electrode. The single electrode potential serves as a useful diagnostic method for assessing the effect of crossover of electrolytes in the cell. In this benchmark case, the separation of reactant in different electrolyte streams has been well maintained.³³ A short-circuit current of 14.7 mA is achieved for this case.

For the scaling up on conventional face-to-face microfluidic configuration, the cell with 6 mm wide channel width only performs a voltage of 1.74 V, with a cathodic potential of 0.76 V and an anodic potential of -0.98 V vs Ag/AgCl. The large difference compared with the anodic potential of cell with 2 mm wide channel indicates the intensification of crossover of the acidic catholyte. With a two-time larger electrode area, the short-circuit currents even decrease from 14.7 mA to 12.7 mA. Conversely, the cell scaled up on the new designed platform to 6 mm width has a similar voltage as that of the cell with 2 mm wide channel. The cathodic and anodic potentials vs Ag/AgCl are 0.75 V and -1.53 V, respectively, indicating a great control on the crossover of different electrolytes. The short-circuit currents increase from 14.7 mA to 37.5 mA by a two-fold increase in area. The distinct difference of the cell performances shows a great advantage in new designed dislocated double-layer structure for scaling up.

Figure 3 shows the cell performance with channel width scaling from 2 mm to 10 mm, with electrolyte flow rate increasing accordingly. As can be seen, the channel width has a slight effect on the OCV (2.26 ± 0.03 V). The anodes and cathodes of the cells with different channel widths show similar potentials vs. Ag/AgCl in open circuit (i.e. -1.55 ± 0.02 V and 0.73 ± 0.03 V, respectively), indicating that the flows of anolyte and catholyte have been well maintained. The polarization curves presented in Figure 3 (a) shows the increase in cell output with larger channel width and larger electrode area. The short-circuit currents increase from 14.7 mA at 2 mm to 55.2 mA at 10 mm. However, the current densities and peak power densities decrease as shown in Figure 3 (b).

The cell with 2 mm wide channel has a short-circuit current density of 147 mA/cm² and a peak power density of 110.04 mW/cm². The performance obtained is significantly advantageous over the cell reported in literature (0.05 to 10 mW/cm²).^{20, 21} When the channel width increases

to 10 mm, the short-circuit current density and peak power density decrease to 110.4 mA/cm² and 67.2 mW/cm², which are 75.1 % and 61.2% of the values in the cell with 2 mm wide channel. Table 2 summarizes the values of OCV, short-circuit current, short-circuit current densities and peak power densities in all the cells tested. The changing of current densities and power densities with channel width is shown in Figure 3 (d). The loss is explained in the EIS analysis section.

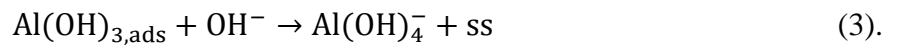
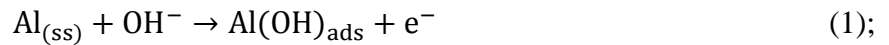
3.2 EIS analysis

3.2.1 Equivalent circuit

During an impedance measurement, the physicochemical processes occurring within the cells have different A.C. signal activated responses, which could be represented by a network of resistors (**R**), capacitors (**C**) and inductors (**L**) in equivalent circuit model to quantify their characteristics. Specialized electrical elements, such as constant phase element (**CPE**) and Warburg element (**W**), are introduced, since real system do not necessarily behave as ideal electrical components.³⁴

For the EIS analysis, electrolyte can be characterized by a resistor **R_E**, representing a conductive pathway for ion transfer. Our previous study have shown that the effects of neutralization on the cell performance can be negligible if the alkali-acid interface is properly controlled.³⁵ Furthermore, the configurations of EIS in Al-air fuel cells with single- and dual-electrolyte are the same, the equivalent circuit model is proposed to be applicable in both cases.

On the side of anode, the oxidation reaction of Al in alkaline solution is described as follows.^{30, 36}



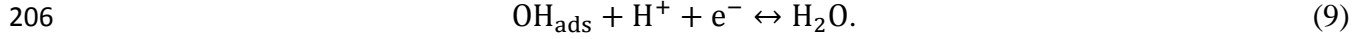
where 'ss' represents a bare Al surface site. The first step of anodic dissolution of Al results in an anhydrous oxide layer on the bare Al surface. The process includes the consumption of Al and formation of Al^+ ions, which would be further oxidized to Al^{3+} in subsequent steps. A capacitor exists due to the existence of a metal/oxide interface. The equivalent elements consist of a charge transfer resistance ($R_{ct,a}$) in parallel with a double-layer capacitance ($C_{dl,a}$). It is a rate determining step in the charge transfer process.²⁹ At the oxide/electrolyte interface, the adsorption process of intermediates (such as OH^- or O^{2-}) results in inductive responses. Corresponding elements are an adsorbed resistance (R_L) and an inductance (L).³⁷ This process is related to electrolyte concentration. The inductive response is not obvious under negative polarization or in KOH electrolyte with higher concentration ($\geq 4 \text{ M}$).³⁸ The growth ($\text{Al}^+ \rightarrow \text{Al}^{3+}$, Equation 2) and dissolution ($\text{Al}(\text{OH})_{3,\text{ads}} \rightarrow \text{Al}(\text{OH})_4^-$, Equation 3) of the hydrous surface film²⁹ result in a low frequency capacity loop, originating from equivalent elements of a charge transfer resistance (R_c) parallel to constant phase capacitance (CPE_a).³⁹ The CPE is employed to compensate for the non-homogeneity.³⁷ The R_c plays an important role in the process of the dissolution of Al oxide film. A higher R_c represents a lower dissolution rate for the Al anode.

At the cathode side, a reduction process of oxygen in alkaline environment occurs as follows:⁴⁰



while in acidic environment:⁴¹





Reduction of O_2 results in two components of charge-transfer resistance ($R_{ct,ch}$ and $R_{ct,cl}$) in parallel with capacitance. The double-layer capacitances are replaced by constant phase elements ($CPE_{c,h}$ and $CPE_{c,l}$), because of the porous structure of the gas diffusion electrode. The high-frequency impedance reflects the combination of a capacitance in the catalyst layer and the effective charge transfer resistance. The low-frequency impedance corresponds to the kinetic impedance of the oxygen reduction reaction.³¹

3.2.2 Fitting and discussion

Based on above reaction mechanism, an equivalent circuit model is proposed as shown in Figure 4. The experimental EIS curves are similar, including a high-frequency capacity loop, a middle-frequency inductive loop and an uncompleted low-frequency capacitive loop, which indicates that the mechanism of the redox processes between Al and oxygen remains the same for all cases. The intercept on the real x -axis at high frequency corresponds to internal cell resistance R_{cell} , which includes both electrolyte solution resistance (R_E), and electrode contacting resistance (R_{Bulk}) ($R_{cell} = R_E + R_{Bulk}$). As shown later, the EIS curves can be fitted well, using the equivalent circuit model described in Figure 4.

3.2.2.1 Verification

The Nyquist plots of the Al-air cells with single- and dual- electrolyte are shown in Figure 5. Parameters of each element in equivalent circuit calculated after fitting are listed in Table 3. As can be observed, cell with dual-electrolyte has a lower overall cell resistance, originated from higher conductivity of H_2SO_4 . According to Table 3, anodic components have similar values in the two cases. The value of $R_{ct,ch}$ in the dual-electrolyte case is much lower than that in single-electrolyte, representing higher reaction rate of the first sub-step of oxygen reduction.

The Nyquist plots of Al-air cells with anolyte of different concentrations are shown in Figure 6. Parameters of each element in the equivalent circuit calculated after fitting are listed in Table 4. As can be seen, cathodic components have quite similar values in the three cases studied. According to Table 4, cells show lower overall cell resistance with higher KOH concentration of anolyte. Resistances of the anodic equivalent elements decrease with the increase of anolyte concentration. $C_{dl,a}$, representing the capacitance on Al surface, increases with higher concentration of KOH. A possible reason for this observation might be the higher concentration of KOH which decreases the thickness of the oxide layer on the Al surface, thereby, increasing the capacitance.

3.2.2.2 Analysis for scaling up (2 mm, 4 mm, 6 mm, 8 mm and 10 mm)

The Nyquist plots of the Al-air cells with different channel widths are shown in Figure 7 and the parameters calculated for fitting are listed in Table 5. During scale-up, the increase in electrode area results in an effective reduction in overall cell ohmic resistance as larger ions conducting path is provided. At the same time, the reaction sites on electrode surface with electrolyte are increased. Therefore, resistances due to the physicochemical processes also decrease with the increase of channel width, giving an explanation for higher performance in cells with larger channel width. However, with the consideration of the electrode area, the resistances per unit area are increased. This is consistent with the result in Figure 3(b). $C_{dl,a}$, which represents the capacitance on the Al surface, increases due to the larger area on the Al surface.

The difference between cells with 8 mm wide channel and 10 mm wide channel is not significant. This is consistent with the slight performance increase from the cells with 8 mm channel to that of 10 mm channel. One thing worth noting is that the Al-air cell suffered from

self-discharging,⁴² leading to hydrogen generation. The amount of hydrogen generated would increase in scaled-up cells, which might affect the result of the test. This phenomenon, however, could be avoided in other cells, such as hydrogen or vanadium cells since gas is not generated in the cells.

4. Conclusion

In this study, we demonstrated the proof of a dislocated double-layer scaling up concept for MFC. The scale-up approach increases the channel dimension of microfluidic fuel cell in four-fold from 2 mm to 1 cm. Within this scaling up platform, the crossover of reactants is well controlled and higher outputs have been obtained by the cells with larger electrode area. The current densities of the scaled-up cell are maintained over 75% with a four-time increase in electrode areas. An EIS analysis on full Al-air cell was conducted for the first time. The equivalent circuit model is validated against the experimental results. Through the impedance fitting results, different resistances were identified, which revealed the electrochemical losses on the cell performance.

In this study, the influences of electrolyte flow rate, concentration and other dimensional parameters were not investigated. Additional improvements are possible by optimization of the operation process. Furthermore, multiplexing scaling up strategy to obtain higher cell power output can be done by combining this direct dimensional scale-up method with porous electrode and cell stacks. With this dimensional scale-up method, other types of cells can be investigated. This method can also be employed in other microfluidic-related fields, such as patterning and T-sensors.

Acknowledgement

The authors would like to acknowledge the support from the Hong Kong Research Grant Council GRF#714313 and SRT on Clean Energy of the University of Hong Kong. We are grateful to Dr. Dong Feifei for the discussion of EIS analyses.

Reference

1. B. C. Steele and A. Heinzl, *Nature*, **414**, 345 (2001).
2. V. Mehta and J. S. Cooper, *Journal of Power Sources*, **114**, 32 (2003).
3. E. Kjeang, N. Djilali and D. Sinton, *Journal of Power Sources*, **186**, 353 (2009).
4. E. R. Choban, L. J. Markoski, A. Wieckowski and P. J. Kenis, *Journal of Power Sources*, **128**, 54 (2004).
5. P. J. Kenis, R. F. Ismagilov and G. M. Whitesides, *Science*, **285**, 83 (1999).
6. A. E. Kamholz, B. H. Weigl, B. A. Finlayson and P. Yager, *Analytical Chemistry*, **71**, 5340 (1999).
7. S. W. Dutse and N. A. Yusof, *Sensors*, **11**, 5754 (2011).
8. S. A. M. Shaegh, N.-T. Nguyen and S. H. Chan, *International Journal of Hydrogen Energy*, **36**, 5675 (2011).
9. J. L. Cohen, D. J. Volpe, D. A. Westly, A. Pechenik and H. D. Abruña, *Langmuir*, **21**, 3544 (2005).
10. S. M. Mitrovski, L. C. Elliott and R. G. Nuzzo, *Langmuir*, **20**, 6974 (2004).
11. A. Li, S. H. Chan and N.-T. Nguyen, *Journal of Micromechanics and Microengineering*, **17**, 1107 (2007).
12. E. R. Choban, P. Waszczuk and P. J. Kenis, *Electrochemical and Solid-State Letters*, **8**, A348 (2005).
13. R. Ferrigno, A. D. Stroock, T. D. Clark, M. Mayer and G. M. Whitesides, *Journal of the American Chemical Society*, **124**, 12930 (2002).
14. J. S. Lee, S. Tai Kim, R. Cao, N. S. Choi, M. Liu, K. T. Lee and J. Cho, *Advanced Energy Materials*, **1**, 34 (2011).
15. B. Ho and E. Kjeang, *Central European Journal of Engineering*, **1**, 123 (2011).
16. E. Kjeang, J. McKechnie, D. Sinton and N. Djilali, *Journal of Power Sources*, **168**, 379 (2007).
17. E. Kjeang, R. Michel, D. A. Harrington, N. Djilali and D. Sinton, *Journal of the American Chemical Society*, **130**, 4000 (2008).
18. K. S. Salloum, J. R. Hayes, C. A. Friesen and J. D. Posner, *Journal of Power Sources*, **180**, 243 (2008).
19. J. W. Lee, J. K. Hong and E. Kjeang, *Electrochimica Acta*, **83**, 430 (2012).
20. D. Fuerth and A. Bazylak, *Journal of Fluids Engineering*, **135**, 021102 (2013).
21. S. Moore, D. Sinton and D. Erickson, *Journal of Power Sources*, **196**, 9481 (2011).
22. K. S. Salloum and J. D. Posner, *Journal of Power Sources*, **196**, 1229 (2011).
23. B. Ho and E. Kjeang, *Journal of Fluids Engineering*, **135**, 021304 (2013).
24. O. A. Ibrahim, M.-A. Goulet and E. Kjeang, *Journal of The Electrochemical Society*, **162**, F639 (2015).
25. L. Renaud, D. Selloum and S. Tingry, *Microfluidics and Nanofluidics*, **18**, 1407 (2015).
26. H. Wang, S. Gu, D. Y. Leung, H. Xu, M. K. Leung, L. Zhang and J. Xuan, *Electrochimica Acta*, **135**, 467 (2014).
27. S. Uhm, S. T. Chung and J. Lee, *Journal of Power Sources*, **178**, 34 (2008).

- 317 28. Z. He and F. Mansfeld, *Energy & Environmental Science*, **2**, 215 (2009).
318 29. K. Emregül and A. A. Aksüt, *Corrosion science*, **42**, 2051 (2000).
319 30. H. Shao, J. Wang, Z. Zhang, J. Zhang and C. Cao, *Journal of Electroanalytical Chemistry*, **549**, 145
320 (2003).
321 31. A. Maghsodi, M. M. Hoseini, M. D. Mobarakeh, M. Kheirmand, L. Samiee, F. Shoghi and M.
322 Kameli, *Applied Surface Science*, **257**, 6353 (2011).
323 32. F. R. Brushett, M. S. Naughton, J. W. D. Ng, L. Yin and P. J. Kenis, *international journal of*
324 *hydrogen energy*, **37**, 2559 (2012).
325 33. B. Chen, D. Y. Leung, J. Xuan and H. Wang, *Energy Procedia*, **75**, 1983 (2015).
326 34. E. Angelini, A. Carullo, S. Corbellini, F. Ferraris, V. Gallone, S. Grassini, M. Parvis and A. Vallan,
327 *Instrumentation and Measurement, IEEE Transactions on*, **55**, 436 (2006).
328 35. X. Lu, J. Xuan, D. Y. Leung, H. Zou, J. Li, H. Wang and H. Wang, *Journal of Power Sources*, **314**, 76
329 (2016).
330 36. M. Doche, J. Rameau, R. Durand and F. Novel-Cattin, *Corrosion science*, **41**, 805 (1999).
331 37. A. Abdel-Gaber, E. Khamis, H. Abo-ElDahab and S. Adeel, *Materials Chemistry and Physics*, **109**,
332 297 (2008).
333 38. L. Fan, H. Lu and J. Leng, *Electrochimica Acta*, **165**, 22 (2015).
334 39. N. Chaubey, V. K. Singh and M. Quraishi, *International Journal of Industrial Chemistry*, **6**, 317
335 (2015).
336 40. H. Huang, W. Zhang, M. Li, Y. Gan, J. Chen and Y. Kuang, *Journal of colloid and interface science*,
337 **284**, 593 (2005).
338 41. O. Antoine, Y. Bultel and R. Durand, *Journal of Electroanalytical Chemistry*, **499**, 85 (2001).
339 42. Z. Zhang, C. Zuo, Z. Liu, Y. Yu, Y. Zuo and Y. Song, *Journal of Power Sources*, **251**, 470 (2014).

Nomenclature

R_E	Electrolyte ohmic resistance	R_{Bulk}	Resistance of electrode bulk and contacting
$C_{dl,a}$	Double-layer capacitance due to the first step of anode oxidation	$R_{ct,a}$	Charge transfer resistance due to the first step of anode oxidation
L	Inductance of adsorption on anode side	R_L	Resistance of adsorption on anode side
CPE_a	Constant phase element due to growth and dissolution of hydrous layer on anode side	R_c	Charge transfer resistance due to growth and dissolution of hydrous layer on anode side
$CPE_{c,h}$	Constant phase element due to the high-frequency response of cathode side	$R_{ct,ch}$	Charge transfer resistance due to the high-frequency response of cathode side
$CPE_{c,l}$	Constant phase element due to the low-frequency response of cathode side	$R_{ct,cl}$	Charge transfer resistance due to the low-frequency response of cathode side

Figure Captions

Figure 1 Schematics of the conventional face-to-face and the new designed dislocated double-layer scaling up Al-air cell structure.

Figure 2 Comparison of the performance between the Al-air fuel cells with conventional face-to-face (▲) and the new designed structure (●) with 6 mm wide channel. The performance of cell with 2 mm wide channel (■) is shown as a benchmark.

Figure 3 Performances of the Al-air fuel cells with dislocated double-layer structure with channel width ranging from 2 mm to 10 mm. (a) Polarization of voltage vs current, (b) Voltage and power density vs current density, (c) Single electrode polarization, of cells with 2 mm (■), 4 mm (●), 6 mm (▲), 8 mm (▼) and 10 mm (◆) channel; (d) Changing of current densities (■) and power densities (●) with channel width.

Figure 4 Schematic of an Al-air cell and its equivalent circuit.

Figure 5 Impedance diagrams (experimental and fitting) of Al-air fuel cells with single- (●), /dual- (■) electrolyte.

Figure 6 Impedance diagrams (experimental and fitting) of Al-air fuel cells with KOH anolyte concentrations of 1 M (■), 2 M (●) and 3 M (▲).

Figure 7 Impedance diagrams (experimental and fitting) of Al-air fuel cells with 2 mm (■), 4 mm (●), 6 mm (▲), 8 mm (▼) and 10 mm (◆) channel widths.

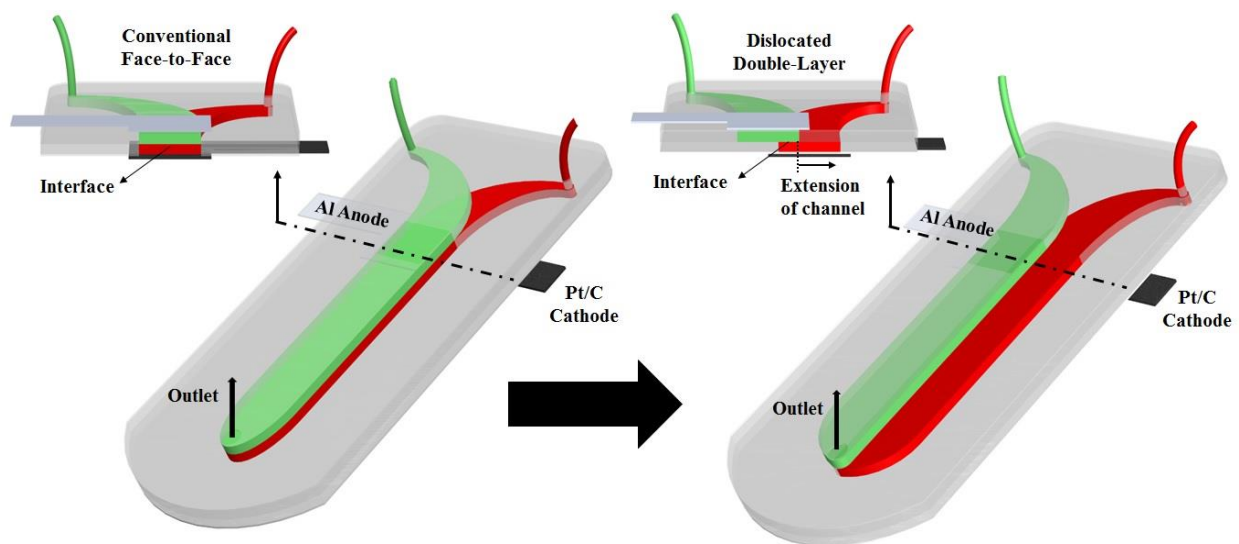


Figure 1 Schematics of the conventional face-to-face and the new designed dislocated double-layer scaling up Al-air cell structure.

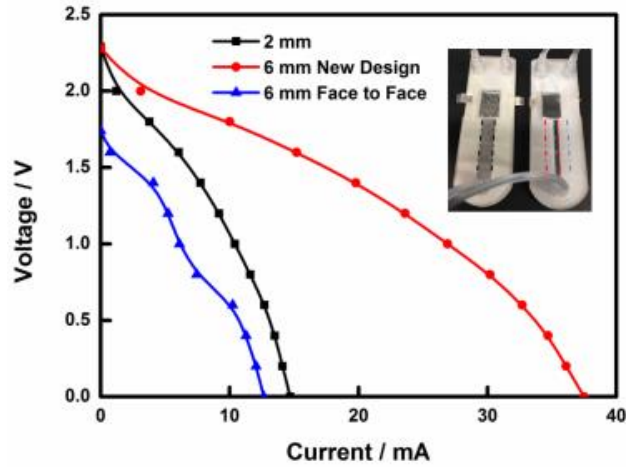


Figure 2 Comparison of the performance between the Al-air fuel cells with conventional face-to-face (▲) and the new designed structure (●) with 6 mm wide channel. The performance of cell with 2 mm wide channel (■) is shown as a benchmark.

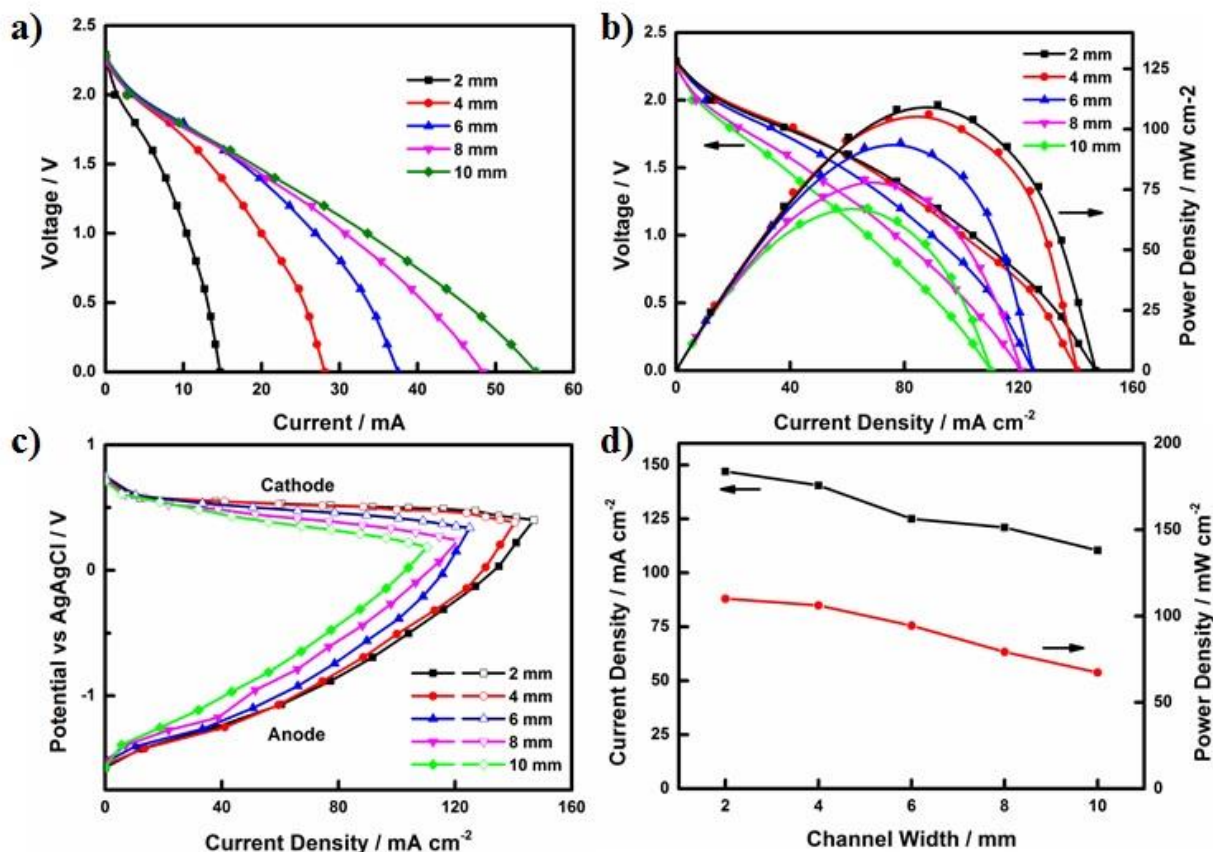


Figure 3 Performances of the Al-air fuel cells with dislocated double-layer structure with channel width ranging from 2 mm to 10 mm. (a) Polarization of voltage vs current, (b) Voltage and power density vs current density, (c) Single electrode polarization, of cells with 2 mm (■), 4 mm (●), 6 mm (▲), 8 mm (▼) and 10 mm (◆) channel; (d) Changing of current densities (■) and power densities (●) with channel width.

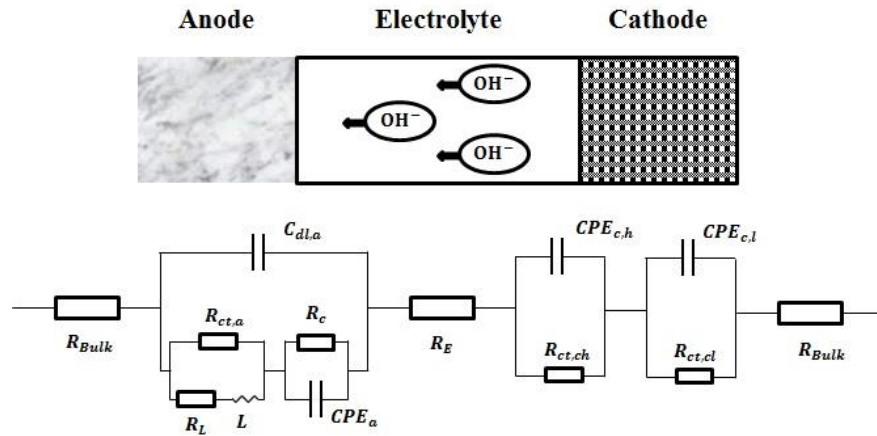


Figure 4 Schematic of an Al-air cell and its equivalent circuit.

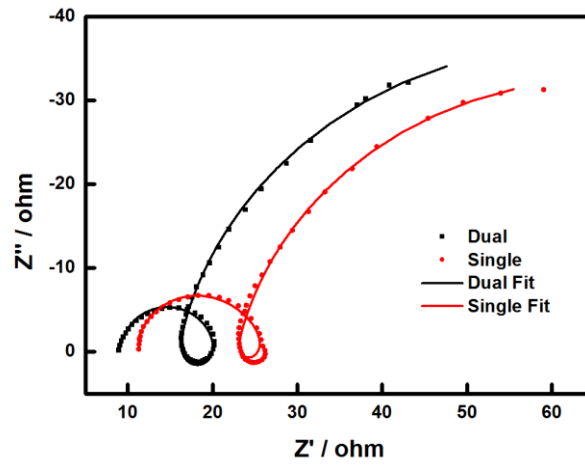


Figure 5 Impedance diagrams (experimental and fitting) of Al-air fuel cells with single- (●) /dual- (■) electrolyte.

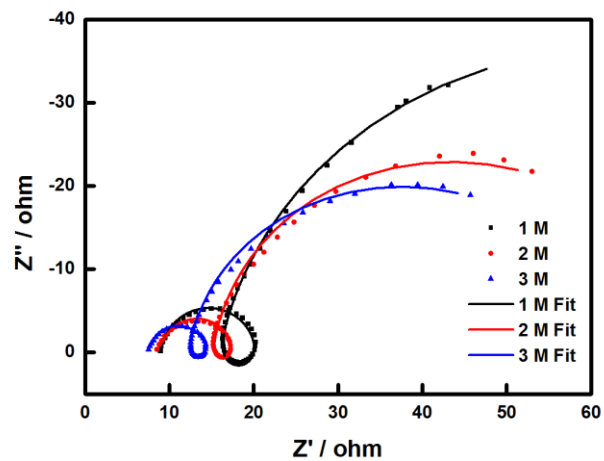


Figure 6 Impedance diagrams (experimental and fitting) of Al-air fuel cells with KOH anolyte concentrations of 1 M (■), 2 M (●) and 3 M (▲).

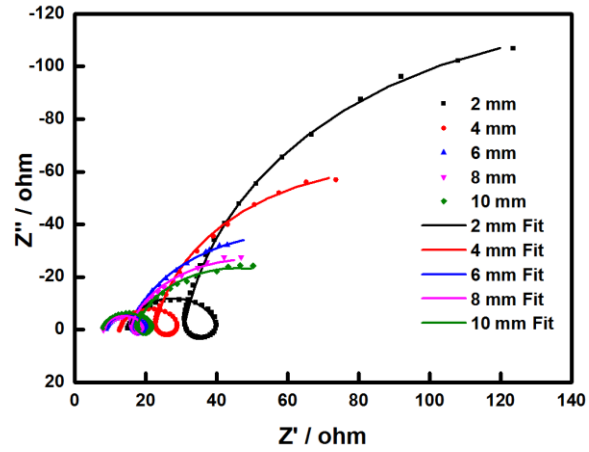


Figure 7 Impedance diagrams (experimental and fitting) of Al-air fuel cells with 2 mm (■), 4 mm (●), 6 mm (▲), 8 mm (▼) and 10 mm (◆) channel widths.

Table 1 Information of the electrolytes for the two groups of EIS verifying test.

		Anolyte (Al)	Catholyte (GDE)
1. Catholyte	Dual	1 M KOH	1 M H ₂ SO ₄
	Single	1 M KOH	1 M KOH
2. Anolyte	Anolyte 1 M	1 M KOH	1 M H ₂ SO ₄
	Anolyte 2 M	2 M KOH	1 M H ₂ SO ₄
	Anolyte 3 M	3 M KOH	1 M H ₂ SO ₄

Table 2 Summary of cell performances shown in Figure 3. Percentages shown in the bracket are from comparison with the values of the 2 mm case.

	2mm	4mm	6mm	8mm	10mm
Flow Rate	600 $\mu\text{l/min}$	1200 $\mu\text{l/min}$	1800 $\mu\text{l/min}$	2400 $\mu\text{l/min}$	3000 $\mu\text{l/min}$
OCV / V	2.289	2.265	2.280	2.240	2.284
$I_{\text{max}} / \text{mA}$	14.7	28.1 (191%)	37.5 (255%)	48.4 (329%)	55.2 (375%)
$i_{\text{max}} / \text{mA cm}^{-2}$	147	140.5 (95.6%)	125 (85.0%)	121 (82.3%)	110.4 (75.1%)
$P_{\text{peak}} / \text{mW cm}^{-2}$	110.04	106.2 (96.5%)	94.4 (85.8%)	79.2 (72.0 %)	67.2 (61.2%)

Table 3 Parameters calculated from the fitting of EIS in Figure 5 with equivalent circuit.

	R_{cell} / Ω	$C_{dl,a} / F$	$R_{ct,a} / \Omega$	R_L / Ω	L / H	R_c / Ω	$CPE_a \cdot T / F$	$R_{ct,ch} / \Omega$	$CPE_{c,h} \cdot T / F$	$R_{ct,cl} / \Omega$	$CPE_{c,l} \cdot T / F$
Single	10.73	1.97×10^{-6}	9.59	8.00	7.86×10^{-3}	40.45	7.78×10^{-3}	7.92	1.74×10^{-4}	38.84	4.28×10^{-3}
Dual	9.00	1.97×10^{-6}	9.29	8.30	8.72×10^{-3}	44.45	7.78×10^{-3}	2.47	3.68×10^{-4}	43.38	4.54×10^{-3}

Table 4 Parameters calculated from the fitting of EIS in Figure 6 with equivalent circuit.

	R_{cell} / Ω	$C_{dl,a} / F$	$R_{ct,a} / \Omega$	R_L / Ω	L / H	R_c / Ω	$CPE_a - T/F$	$R_{ct,cl} / \Omega$	$CPE_{c,h} - T/F$	$R_{ct,cl} / \Omega$	$CPE_{c,l} - T/F$
Anolyte 1M	9.00	1.97×10^{-6}	9.29	8.30	8.72×10^{-3}	44.45	7.78×10^{-3}	2.47	3.68×10^{-4}	43.38	4.54×10^{-3}
Anolyte 2M	8.79	2.14×10^{-6}	6.48	7.71	4.33×10^{-3}	16.32	3.99×10^{-3}	2.72	2.15×10^{-4}	41.93	4.58×10^{-3}
Anolyte 3M	7.46	2.40×10^{-6}	4.96	3.88	2.29×10^{-3}	10.98	5.12×10^{-3}	2.58	2.62×10^{-4}	40.38	4.54×10^{-3}

608 **Table 5** Parameters evaluated from fitting of EIS in Figure 7 with equivalent circuit.

	R_{cell} / Ω	$C_{\text{dl,a}} / \text{F}$	$R_{\text{ct,a}} / \Omega$	R_{L} / Ω	L / H	R_{c} / Ω	$\text{CPE}_{\text{a}} \cdot T$	$R_{\text{ct,ch}} / \Omega$	$\text{CPE}_{\text{c,h}} \cdot T / \text{F}$	$R_{\text{ct,cl}} / \Omega$	$\text{CPE}_{\text{c,l}} \cdot T / \text{F}$
2 mm	15.48	9.73×10^{-7}	21.48	10.55	1.36×10^{-2}	145.70	1.28×10^{-3}	8.81	3.97×10^{-4}	145.00	4.14×10^{-3}
4 mm	12.95	1.91×10^{-6}	13.62	8.73	9.82×10^{-3}	69.68	2.72×10^{-3}	4.45	3.61×10^{-4}	77.36	5.66×10^{-3}
6 mm	9.00	1.97×10^{-6}	9.29	8.30	8.72×10^{-3}	44.45	7.78×10^{-3}	2.47	3.68×10^{-4}	43.38	4.54×10^{-3}
8 mm	8.59	2.44×10^{-6}	9.05	7.17	8.65×10^{-3}	29.54	9.38×10^{-3}	3.06	6.12×10^{-4}	35.65	4.68×10^{-3}
10 mm	8.16	1.51×10^{-6}	10.84	6.12	9.88×10^{-3}	19.71	9.02×10^{-3}	5.28	4.13×10^{-4}	36.26	4.10×10^{-3}

609